The substorm cycle as reproduced by global MHD models

E. Gordeev[1] , V. Sergeev[1] , N. Tsyganenko[1] , M. Kuznetsova[2], L. Rastäetter[2] , J. Raeder[3] , G. Tóth[4] , J. Lyon[5] , V. Merkin[6] , and M. Wiltberger[7]

[1] Earth Physics Department, Saint-Petersburg State University, St. Petersburg, Russia, [2] NASA Goddard Space Flight Center, Greenbelt, Maryland, USA, [3] Space Science Center, University of New Hampshire, Durham, New Hampshire, USA, [4] Center for Space Environment Modeling, University of Michigan, Ann Arbor, Michigan, USA, [5] Department of Physics and Astronomy, Dartmouth College, Hanover, New Hampshire, USA, [6] Applied Physics Laboratory, The Johns Hopkins University, Laurel, Maryland, USA, [7] High-Altitude Observatory, National Center for Atmospheric Research, Boulder, Colorado, USA

Abstract Recently, Gordeev et al. (2015) suggested a method to test global MHD models against statistical empirical data. They showed that four community-available global MHD models supported by the Community Coordinated Modeling Center (CCMC) produce a reasonable agreement with reality for those key parameters (the magnetospheric size, magnetic field, and pressure) that are directly related to the large-scale equilibria in the outer magnetosphere. Based on the same set of simulation runs, here we investigate how the models reproduce the global loading-unloading cycle. We found that in terms of global magnetic flux transport, three examined CCMC models display systematically different response to idealized 2 h north then 2 h south interplanetary magnetic field (IMF) B_z variation. The LFM model shows a depressed return convection and high loading rate during the growth phase as well as enhanced return convection and high unloading rate during the expansion phase, with the amount of loaded/unloaded magnetotail flux and the growth phase duration being the closest to their observed empirical values during isolated substorms. Two other models exhibit drastically different behavior. In the BATS-R-US model the plasma sheet convection shows a smooth transition to the steady convection regime after the IMF southward turning. In the Open GGCM a weak plasma sheet convection has comparable intensities during both the growth phase and the following slow unloading phase. We also demonstrate potential technical problem in the publicly available simulations which is related to postprocessing interpolation and could affect the accuracy of magnetic field tracing and of other related procedures.

1. Introduction

The Earth's magnetosphere provides a great challenge for researchers because of its inhomogeneous, structured, and extremely variable nature. Numerical simulations provide the only opportunity to follow the complicated evolution of the entire complex system, controlled by its ever changing multiparametric driver, the solar wind. Of all the available first-principle-based approaches, the global MHD (GMHD) models have a special place due to their ability to simulate the entire solar wind-driven magnetosphere at a low computational cost. However, because of their neglect of the kinetic aspects, they are unable to correctly describe the drift-dominated inner magnetosphere, as well as such important details of the systems response as the substorm onset time and location [*Kuznetsova et al.*, 2007]. There were attempts to incorporate a more sophisticated physics into the GMHD models, e.g., by locally including particle effects into the large-scale GMHD description of the system [*Toffoletto et al.*, 2005; *Pembroke et al.*, 2012; *Daldorff et al.*, 2014; *Ashour-Abdalla et al.*, 2015]. However, none of them provided a cost-effective solution to replace the GMHD models for operational purposes and community-available research. Also, the addition of particle physics does not always improve the results of testing the models against data [*Pulkkinen et al.*, 2011; *Honkonen et al.*, 2013]. In addition, the GMHD simulations by themselves are still far from being a routine tool: there exist a dozen of different models worldwide, and quite often (see examples below) they provide widely different results on the system behavior and its parameter values. Therefore, the quantitative assessment and validation of the MHD component of global magnetospheric models against the reality still remains a critical but difficult issue.

Dozens of particular validation studies have been published so far. However, there exists no commonly accepted optimal methodology on how to compare the GMHD models against the reality. Most of the past validation attempts were separately applied to particular solar wind conditions or to particular magnetospheric

parameter(s) measured at some particular locations. Recently, *Gordeev et al.* [2015] (referred henceforth as G15) suggested a different procedure of the model benchmarking and tested it on four community-available GMHD codes operated by the NASA Community Coordinated Modeling Center (CCMC). The basic components of that approach are as follows. (1) Evaluate principal global variables (the state parameters or key magnetospheric parameters) that quantitatively characterize the most important elements of the system structure and dynamics and compare their model values with observations; (2) use statistical empirical relationships to validate the model predictions, rather than observations along particular spacecraft orbits made at specific times; (3) cover the most probable ranges of the solar wind input parameter values and avoid basing the metrics on regions or phenomena which (by their nature and the simulation design) are inaccurately reproduced by the GMHD model (e.g., the inner magnetosphere, ionospheric currents, and ground magnetic perturbations). Using of quantitative scores in a carefully designed statistical comparison of model predictions and observations provides an objective quantitative measure of a particular model's performance. The G15 results have confirmed that all the GMHD models operated at CCMC (BATS-R-US, LFM, Open GGCM, and GUMICS) are able to simulate the large-scale magnetospheric structure. They reasonably well predict the absolute values and average SW-induced variations for those key parameters that characterize the magnetospheric size, magnetic field/flux, and plasma pressure in the tail. These global parameters are directly related to the large-scale magnetospheric equilibria in the outer magnetosphere, which is supposed to be correctly described by the MHD approach. At the same time, the results for some other parameters, such as the global convection, total field-aligned current, or the magnetotails ability to store the magnetic flux after the north-south IMF turning, provided very diverse answers among four models. In this paper, we use the same set of simulations (except for GUMICS simulations) and focus on the ability of the models to reproduce the most important aspects of magnetospheric dynamics: the magnetic flux transfer and the substorm-related loading-unloading cycle, which represents a principal large-scale perturbation in the magnetosphere and has important space weather implications [*McPherron*, 1991].

A fundamental concept in the large-scale magnetospheric dynamics is the magnetic flux circulation scheme, proposed by *Dungey* [1961] and further extended to nonsteady state by *Russell and McPherron* [1973], *Semenov and Sergeev* [1981], *Siscoe and Huang* [1985], *Cowley and Lockwood* [1992], and many others, in application to the substorm process. Many observations in different magnetospheric domains have demonstrated the validity of the global circulation paradigm and the loading-unloading substorm cycle. Those include the magnetotail magnetic field measurements [*Russell and McPherron*, 1973; *Baker et al.*, 1996; *McPherron*, 1991; *Shukhtina et al.*, 2005; *Angelopoulos et al.*, 2013] as well as in the ionospheric observations of convection patterns and polar cap size change [*Provan et al.*, 2004; *Milan et al.*, 2007; *DeJong et al.*, 2009; *Clausen et al.*, 2013]. Recently, the combined measurements of GPS receivers and SuperDARN radars made it possible to trace the entire Dungey cycle by having observed the convection of plasma irregularities in the high-latitude ionosphere [*Zhang et al.*, 2015].

According to the concept of nonstationary Dungey cycle, different magnetospheric states result from the imbalance between the dayside and nightside reconnection rates. In particular, during the substorm growth phase the dayside reconnection rate is much larger than the nightside one [*Milan et al.*, 2007], which results in accumulation of the magnetotail magnetic flux (F_T), current sheet thinning, and overall stretching of the tail configuration [*Baker et al.*, 1996]. The net F_T increase by the end of the growth phase corresponds to the amount of the magnetic flux that may be potentially reconnected during the substorm expansion phase, when the nightside reconnection rate abruptly increases and exceeds the intake rate on the dayside, resulting in the F_T reduction [*Yahnin et al.*, 2006; *Milan et al.*, 2007; *Shukhtina et al.*, 2014]. Complementary to the magnetotail magnetic flux (global parameter, which is relatively easy to monitor in the GMHD simulations) are the electric potential drops, which provide information about the global flux transport (and dissipation) rates in different parts of the magnetosphere. Combining these global state parameters allows us to quantitatively characterize the global flux transfer in the GMHD models. From four GMHD models supported by the CCMC (BATS-R-US [*Powell et al.*, 1999; *Toth et al.*, 2012], Open GGCM [*Raeder et al.*, 2008], LFM [*Lyon et al.*, 2004; *Merkin and Lyon*, 2010], and GUMICS [*Janhunen et al.*, 2012]), only the first three have been tested in this work. As detailed in G15, the GUMICS model was found to provide much lower flux transport and loading rates than other models for this particular set of low-resolution simulations (see the lobe magnetic field and cross-polar cap potential drop values and variations in Figures 1 and 8 in G15, which can serve as indicators of magnetic flux transport behavior in the system), and this is why it was not included in the present study.

2. The Set of Simulations and Computation of Global Parameters

In this study we use the same set of artificial event simulations as described in *Gordeev et al.* [2015]. The global numerical models solve similar system of ideal MHD equations, but they may significantly differ in numerical implementation details: the type and order of numerical scheme, type of spatial grid, boundary conditions, and others. A summary of the main characteristics of GMHD models used in our study can be found in Table S1 in the supporting information. The simulations have been done for comparable (medium) grid resolution (e.g., in the plasma sheet at $X = -10\,R_E$: BATS-R-US−0.25 R_E, GUMICS−0.5 R_E, LFM−0.8R_E, Open GGCM−0.3 R_E, see more details in Table S1 in the supporting information) and also tested with more fine grids, with no dipole tilt, and constant ionospheric conductance, using the same set of inputs for all four GMHD models. A set of 19 IMF input sequences was devised, each containing 2 h long northward IMF interval followed by 2 h long southward IMF interval—see an example in Figure 2 later in the paper. All other SW parameters were fixed during each particular 4 h long simulation, but their values (as well as the amplitudes of northward and southward IMF) varied between different simulations to reproduce the statistical distribution of main solar wind driver variables, such as SW dynamic pressure and SW electric field. Table S2 provides all SW/IMF input parameters as well as the names of corresponding runs, which can be found in the CCMC database (https://ccmc.gsfc. nasa.gov/). Such a design of synthetic inputs has several advantages. First, it allows one to cover the actual range of many SW/IMF input parameters (and explore their effects) at relatively low computational costs. Second, the northward-then-southward IMF sequence represents the well-known condition leading to substorms [*McPherron*, 1991; *Baker et al.*, 1996; *Milan et al.*, 2007], so this simulation set allows us to investigate the generation of substorm loading/unloading sequence for different values of input parameters, including different levels of northward B_z, plasma pressure, and velocity prior to the event. The time resolution of the GMHD output was chosen as high as 1 min during the first hour of southward IMF in each simulation (and 5 min in the rest of the simulation), which allows an accurate timing of magnetotail changes to be made during the GMHD substorm.

A cornerstone of G15 validation approach is to investigate statistically the global key variables, which characterize the large-scale magnetospheric state and dynamics, rather than to study some particular parameters observed along specific orbits for particular events. This allows us to concentrate on most essential and principal characteristics/processes of global scale and significance. For the MHD description (frozen-in plasma), which is expected to be valid in the outer magnetosphere, magnetosheath, and solar wind, the magnetotail magnetic flux and global flux transport rate represent such natural global variables.

To identify and quantitatively characterize the substorm cycle in the simulations, we use the total magnetic flux in the magnetotail (F_T). As a traditional measure of the global convection strength we use the cross-polar cap electric potential (CPCP) in the ionosphere, which is routinely provided by the CCMC tools and represents the difference between the maximum and minimum values of the electric potential in the high-latitude ionosphere (here in the Northern Hemisphere). As shown in *Gordeev et al.* [2011] the CPCP is basically contributed by the dayside-merging integral rate; therefore, it can serve as a proxy of the dayside-merging key parameter. As a measure of the flux transport rate in the plasma sheet, a cross-tail electric potential in the tail plasma sheet (CTP) was calculated in the $X = -15\,R_E$ magnetotail cross section by integrating the electric field ($E = -V \times B$) y component in the equatorial plane, the integration was performed along the Y axis between $Y = -15\,R_E$ and $Y = +15\,R_E$, that is

$$\text{CTP} = -\int_{-15}^{+15} (\boldsymbol{V} \times \boldsymbol{B})_y \mathrm{d}y \qquad (1)$$

As an integral measure of the magnetic flux transport along the tail, the CTP parameter was found to only weakly depend on X, i.e., to be insensitive to the location of the reconnection line. We have quantitatively verified and confirmed that fact at a set of locations between $X = -12$ and $-25\,R_E$.

The F_T value is calculated in the same YZ tail cross section at $X = -15\,R_E$ by integrating the magnetic field x component in the tail cross section confined by the magnetopause and equatorial plane, that is

$$F_T = -\int_S B_x \mathrm{d}s \qquad (2)$$

The distance $15R_E$ is the optimal choice, since here the configuration is taillike and the grid resolution in the models is still good compared to larger distances.
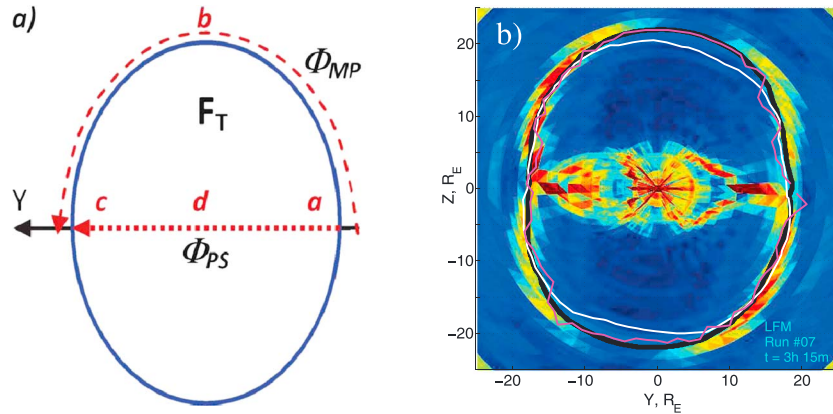
Figure 1. (a) Illustration of basic variables (F_T, Φ_{PS}, and Φ_{MP}) calculated in the *YZ* tail cross section which help to characterize the global flux transfer; (b) example of current density distribution in the simulated tail cross section at $X = -15\,R_E$ (color) in LFM simulation; three curves show the magnetopause position obtained by different methods including fluopause (white), as well as based on mass flux (black) and density gradient (magenta). Note a good agreement between mass flux and density- and current-based local magnetopause determinations and that the fluopause stays inward from other proxies by $1-2\,R_E$.

A critical part of the F_T calculation is the magnetopause identification. It can be defined in the simulated magnetosphere by finding either the peak of electric current or the maximum of plasma density (or thermal pressure) gradient, or using the combination of these two [*Garcia and Hughes*, 2007]. These methods are computationally cheap, but they usually fail at low latitudes where the field and plasma gradients are more distributed and structured. Following *Palmroth et al.* [2003], in most of recent studies [*Gordeev et al.*, 2011; *C. Wang et al.*, 2014], the authors identified the GMHD magnetopause as the fluopause surface, i.e., the innermost boundary of the plasma streamlines coming from the solar wind and enclosing the magnetospheric cavity. The fluopause method is robust and it gives a smooth magnetopause proxy in both high and low latitudes. However, in our experience, the fluopause may have difficulties related to the nonlocal nature of the method: while moving along the magnetosheath, the solar wind plasma also penetrates into the magnetosphere, thus giving rise to the plasma mantle, which is located inside the lobes, convects inward, and eventually reaches the plasma sheet somewhere at distances $\sim 60-150\,R_E$ [*Pilipp and Morfill*, 1978; *C.-P. Wang et al.*, 2014]. From the viewpoint of computational costs, the fluopause method is quite expensive, as it usually requires to trace thousands of streamlines at each step.

In this paper, to find the magnetopause, we use a different approach. As suggested by *Peng et al.* [2010] and confirmed in our extensive testing using big simulation data set for three GMHD models, the locations where the particle mass flux (mNV) is reduced to half of its initial value in the solar wind can be considered as a good proxy for the magnetopause position. That simple method is based on the basic MHD variables, does not require to compute derivatives or trace the flowlines, is local, computationally cheap, and gives a smooth and well-defined surface whose location is in good agreement with other local methods—see Figure 1b for the illustration and Appendix A for more details on the method and its comparison to other methods.

Three above defined global variables help us control the global magnetic flux transport in the system and identify the GMHD analogies for the substorm phases. As discussed by *Semenov and Sergeev* [1981] and *Siscoe and Huang* [1985], the magnetic flux variation in the tail cross section obeys the Faraday law, which gives a simple relationship for a contour *abcda* encircling the northern half of the tail cross section as shown in Figure 1a:

$$dF_T/dt = \Phi_{MP} - \Phi_{PS} \tag{3a}$$

$$\Phi_{MP} = \int_{abc} \boldsymbol{E} \cdot d\boldsymbol{l} = -\int_{abc} [\boldsymbol{V} \times \boldsymbol{B}]_t \, dl \tag{3b}$$

$$\Phi_{PS} = \int_{adc} E_y \, dy \tag{3c}$$

Here the electric field circulation along the closed contour is split into two parts. One part (Φ_{MP}) integrates tangential *E* field along the magnetopause from dawn to dusk, it represents a solar wind dynamo,

indicating magnetic flux transport from the dayside magnetosphere into the magnetotail. We may think of cross-polar cap potential in the ionosphere (CPCP) as a proxy of dayside reconnection potential in the simulations [*Siscoe et al.*, 2001; *Gordeev et al.*, 2011]. Another part (Φ_{PS}) represents an integral measure of the plasma sheet convection and is roughly proportional to the total dissipation rate ($\int E_y J_y dy$) in the plasma sheet. Its proxy in our simulation is provided by the CTP parameter.

3. Large-Scale Dynamics Observed in the GMHD Simulations

Figure 2 illustrates the simulated behavior of F_T, CTP, and CPCP global variables observed in three GMHD models for two different input sequences (#3 and #8), which both have a comparable solar wind merging E field ($E_{KL} = V_{SW} B t_{SW} \sin^2(\theta/2)$ of ~3 mV/m) and are expected to have similar loading-unloading rates. An obvious conclusion is that three GMHD codes provide systematically different magnetospheric reaction under the same driver intensity. In particular, the amount of magnetic flux in the tail and the level of magnetospheric and ionospheric convection may differ by several times between the models. Also, there are visible differences in the dynamics of their behavior after the southward turning of IMF at $t = 120$ min. An example of time sequence of meridional and equatorial views of the magnetic field, flow pattern, pressure, and flux transport in these three models is presented in supporting information movies.

A simple picture based on equation (3) and Figure 1a is useful as a guide in our efforts to identify the GMHD substorm. In the case of idealized sequence of the IMF variation, the first 2 h long time interval of northward IMF is expected to provide a quiet presubstorm background, with low Φ_{MP} (CPCP), Φ_{PS} (CTP), and dF_T/dt, which is the case in all examples shown in Figure 2. Following the arrival of southward IMF to the subsolar magnetopause and enhancement of the dayside reconnection, one expects (and observes, see Figure 2) the CPCP growth and associated increase of Φ_{MP}, implying the loading of the reconnected flux tubes to the magnetotail. The actual behavior of dF_T/dt depends on the balance between the loading of the flux tubes into the lobes from dayside Φ_{MP} and the plasma sheet convection rate Φ_{PS} which returns the plasma tubes back to the dayside. The most effective loading during the growth phase is expected in the case of no convection ($\Phi_{PS} = 0$) when all the loaded magnetic flux is accumulated in the tail, so that $dF_T/dt = \Phi_{MP}$ [*Semenov and Sergeev*, 1981]. In terms of our variables, this should correspond to the situation of low CTP and fast F_T growth, which appears to be realized in LFM simulations (blue curves in Figure 2). In case of strongly enhanced plasma sheet convection and dissipation ($\Phi_{PS} > \Phi_{MP}$), one expects to see the unloading of the tail flux ($dF_T/dt < 0$). This is usually associated with enhanced reconnection in the midtail region, accompanied by many other related dissipative phenomena which in combination characterize the substorm expansion phase. Such contrasted behavior of the plasma sheet convection during the growth and expansion phase of substorms is systematically observed in the midtail plasma sheet [*Nakamura et al.*, 1999; *Dmitrieva et al.*, 2004]. In these examples, the LFM simulation provides the most contrasting example of substorm phases in the CTP parameter. Let us examine the outputs of three models in more detail.

A sharp increase of the ionospheric convection (CPCP) after $t = 120$ min is seen in all models but with different amplitudes. The CPCP amplitude is close to its empirical values in BATS-R-US and is enhanced by a factor of 2 and 2.5 in LFM and Open GGCM models, respectively (see statistical results in Figure A2 of G15). The magnetic flux enhancements during the substorm growth phase differ significantly between the models both in their duration and amplitude. F_T increases by about a factor of 3 (from 0.27 GWb to 0.74 GWb) during 45 min in the LFM model, while it gains ~40% (0.39 GWb to 0.60 GWb) during a short 30 min growth phase in the BATS-R-US model. In its turn, the Open GGCM starts from twice higher F_T (0.53 GWb) and within 70 min increases the amount of the lobe flux by ~60% to 0.84 GWb.

Examination of the cross-tail potential complements the interpretation of the tail flux variations. Contrary to the expected depressed plasma sheet convection during the growth phase, in Open GGCM simulations the CTP increases to several tens of kV in several minutes after the start of the magnetic flux loading to the tail or even prior to it. After that it continues to rise together with F_T, indicating the enhanced convection and dissipation in the plasma sheet. In the BATS-R-US simulations the CTP steadily increases soon after the start of F_T loading, and in ~25 min after that it reaches the level of several tens of kV, corresponding to the peak strength of plasma sheet convection and dissipation attained during the simulation. In both the models, the obtained variations resemble the smooth transition between two quasi-steady states. After a weak enhancement, the CTP value in all the LFM simulations remains suppressed at low level (compared to *CPCP*) during the growth phase, until its sharp increase which indicates the start of the expansion phase
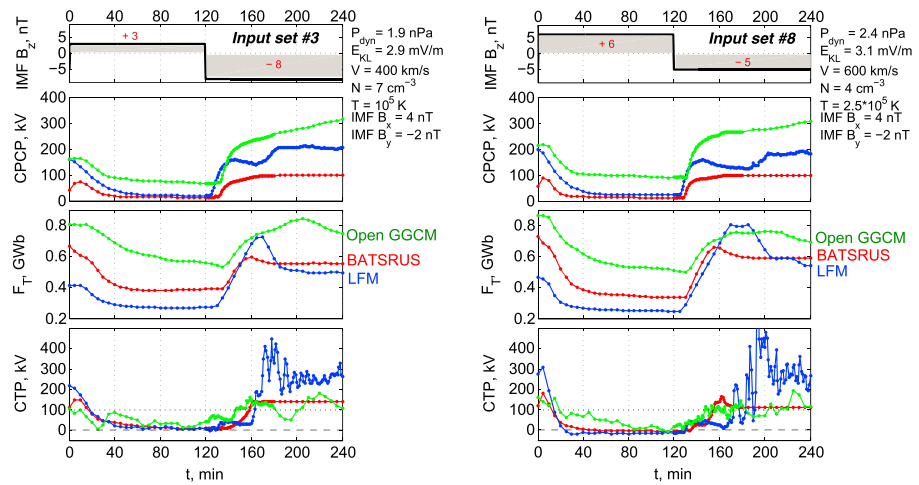
Figure 2. Example of solar wind input (set #3 and #8) and comparisons of outputs of three GMHD models; shown are the global magnetospheric parameters: cross-polar cap potential, tail magnetic flux, and cross-tail potential at $X = -15\,R_E$.

(here the CTP values are several times larger than the CPCP level) closely resembling the idealized substorm behavior as described by *McPherron* [1991], *Baker et al.* [1996], *Shukhtina et al.* [2005], and *Milan et al.* [2007].

Now we compare quantitatively the global behavior with the empirical data. This is not a simple task, because both the F_T and CTP variables are not directly measurable, so no empirical relations are available for them. For that purpose we use two related characteristics, both characterizing the global system behavior. One of them is the duration of the growth phase. From simulations, the growth phase onset time T_s is defined as the start time of lobe magnetic field increase, and the growth phase end (or expansion onset) time T_e is defined by the time when B_L reaches its maximum, thus giving $T_{GP} = T_e - T_s$. From observations (see Appendix B for more detail), during isolated substorms T_s is identified as the onset of polar cap convection (PC index) growth, whereas the expansion onset time T_e is taken from sudden intensification of the auroral zone westward electrojet (of the SML index, see *Newell and Gjerloev* [2011]). Comparison of modeled and empirical growth phase durations as a function of solar wind-induced merging electric field (E_{KL}) is presented in Figure 3a.

Another useful characteristic of the loading rate is provided by the variations of the lobe magnetic field $B_L(t)$ taken at the reference point $(-15,0,10)\,R_E$. In the model we define the lobe field increase rate as the difference of B_L values taken at the times close to T_e and T_s, divided by this duration (that is $dB_L/dt = (B_e - B_s)/T_{GP}$). For comparison we need the statistical empirical relationship of dB_L/dt reduced to the reference point and
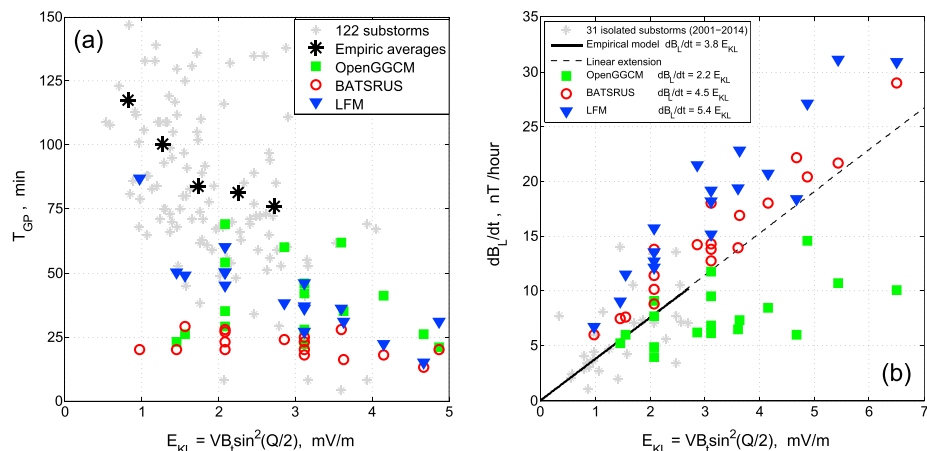
Figure 3. Analysis of the (a) growth phase duration and (b) lobe magnetic field loading rate as a function of the merging electric field E_{KL} in three GMHD models compared with the empirical data. Grey points show the spread of individual events, black stars indicate the derived average values, black lines in Figure 3b correspond to the average linear slope in the observation-based relationships.

expressed as a function of the solar wind electric field. Since no such relationship was available from previous studies (except from that of *Rybalchenko and Sergeyev* [1985]), this was derived from analyses of the lobe magnetic field measurements combined with the OMNI data base solar wind data (see Appendix B for the information about the procedure and results). Comparison of modeled and empirical loading rates as a function of solar wind electric field (E_{KL}) is presented in Figure 3b for the lobe magnetic field.

The range and distribution of empirical T_{GP} values in Figure 3a as well as their decreasing trend with the increasing E_{KL} magnitude are similar to those found in previous studies [*Dmitrieva and Sergeev*, 1983; *Petrukovich*, 2000; *Li et al.*, 2013]. The LFM model clearly reproduces the T_{GP} dependence on E_{KL}, while there is a strong scatter in the Open GGCM output. The growth phase duration in both MHD models is typically by ~20–30% shorter than the average empirical values. In the BATS-R-US model the loading duration is short (~25 min) and almost independent on E_{KL}.

As concerns the lobe magnetic field increase rate during the growth phase, all models show its growth with the increase of dayside merging rate proxy E_{KL} as required by the Faraday law in equation (3). Compared to empirical estimates, the LFM provides a ~30–40% larger B_L increase, it compensates the shorter growth phase duration, and may provide the realistic total loaded flux. In Open GGCM the growth rate is ~30% smaller than the empirical estimate, so the total loaded flux should be somewhat underestimated. The BATS-R-US model provides the loading rate only slightly higher than empirical but similarly should underestimate the loaded flux because of very short loading duration.

As concerns the unloading stage, three models show some unloading during a 2 h southward IMF direction simulation interval, but again it shows significant differences. There are distinct discrepancies in the onset F_T value, unloading rate and duration, and consequently the amount of magnetic flux removed from the tail. Two artificial events shown in Figure 2 demonstrate very modest flux unloading in Open GGCM simulations (from 0.85 to 0.75 GWb, 12%, and from 0.76 to 0.69 GWb, 9%), and in the BATS-R-US simulations (from 0.60 to 0.55 GWb, 8%, and from 0.66 to 0.59 GWb, 11%). However, the flux removal is much larger in the LFM simulations (from 0.73 to 0.50 GWb, or 32%, and from 0.81 to 0.59 GWb, 27%). There are also significant quantitative and qualitative differences between models concerning the level and appearance of the plasma sheet convection in the plasma sheet, this will be discussed at more length in the next section.

4. Average Behavior of Global Variables

To characterize statistically the global behavior and to compare average parameters of magnetic flux loading/unloading with their previously published estimates, we present the superposed epoch analysis for 19 GMHD substorms. As a reference point to construct the Figure 4 we use the time of the tail flux peak at $X = -15\,R_E$. In a visual way these results reveal significant and systematic differences in the behavior of the tail magnetic flux and plasma sheet convection as described by three GMHD models. The large contrast between the growth and expansion phases is present in the LFM simulations: in that model the plasma sheet convection is significantly depressed/enhanced (roughly, the CTP is 30 kV and 280 kV), which is reflected in the largest rates of magnetic flux loading/unloading compared to other models. Quite differently, the Open GGCM shows that the plasma sheet convection and dissipation starts soon after the southward turning and continues at roughly the same level throughout the growth and expansion phase (both at ~100 kV for CTP average levels). It demonstrates the smallest contrast between two phases and the smallest average loading/unloading rates among the three models (see also Figure 3b). In the BATS-R-US simulations, the growth phase has a shortest duration (~25 min, see also Figure 3a), and during that time interval the plasma sheet convection is steadily increasing. In the BATS-R-US simulations there is no similarity to the behavior expected during substorms: there is very little unloading and the plasma sheet convection is not enhanced significantly during the expansion phase (after $T = 0$) compared to the final growth phase; here the earthward convection (CTP) starts to grow steadily during the very short growth phase, as has been already discussed above.

Quantitatively, on the average the BATS-R-US model shows the flux unloading from 0.60 to 0.57 GWb (5%) during the first 15 min after $T = 0$, with no change afterward. Average tail flux unloading in Open GGCM starts from higher value of $F_T = 0.77$ GWb, and the magnetic flux decreases to 0.71 GWb (8%) during next 60 min. In the LFM simulations during ~50 min long substorm expansion, the F_T decreases from 0.71 to 0.49 GWb (31%); most of this unloading occurs during first 30 min after $T = 0$.
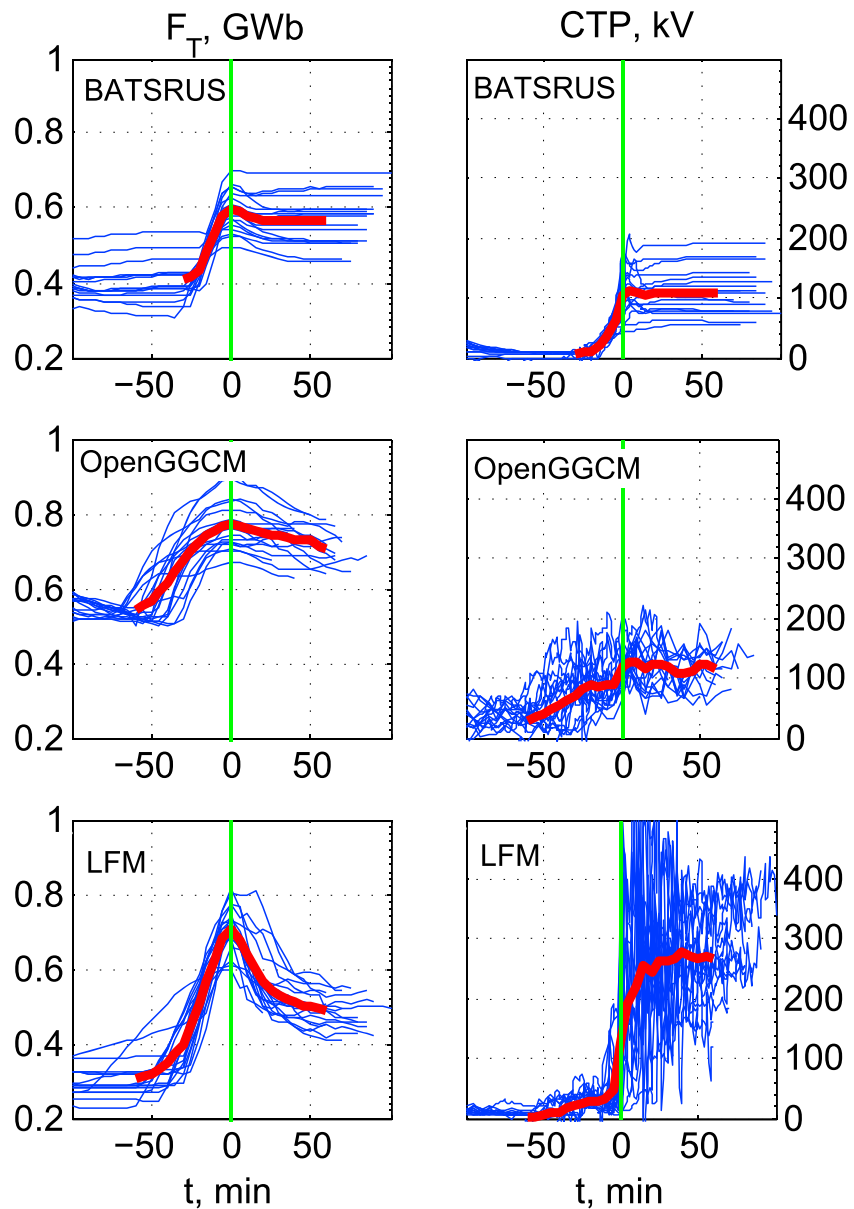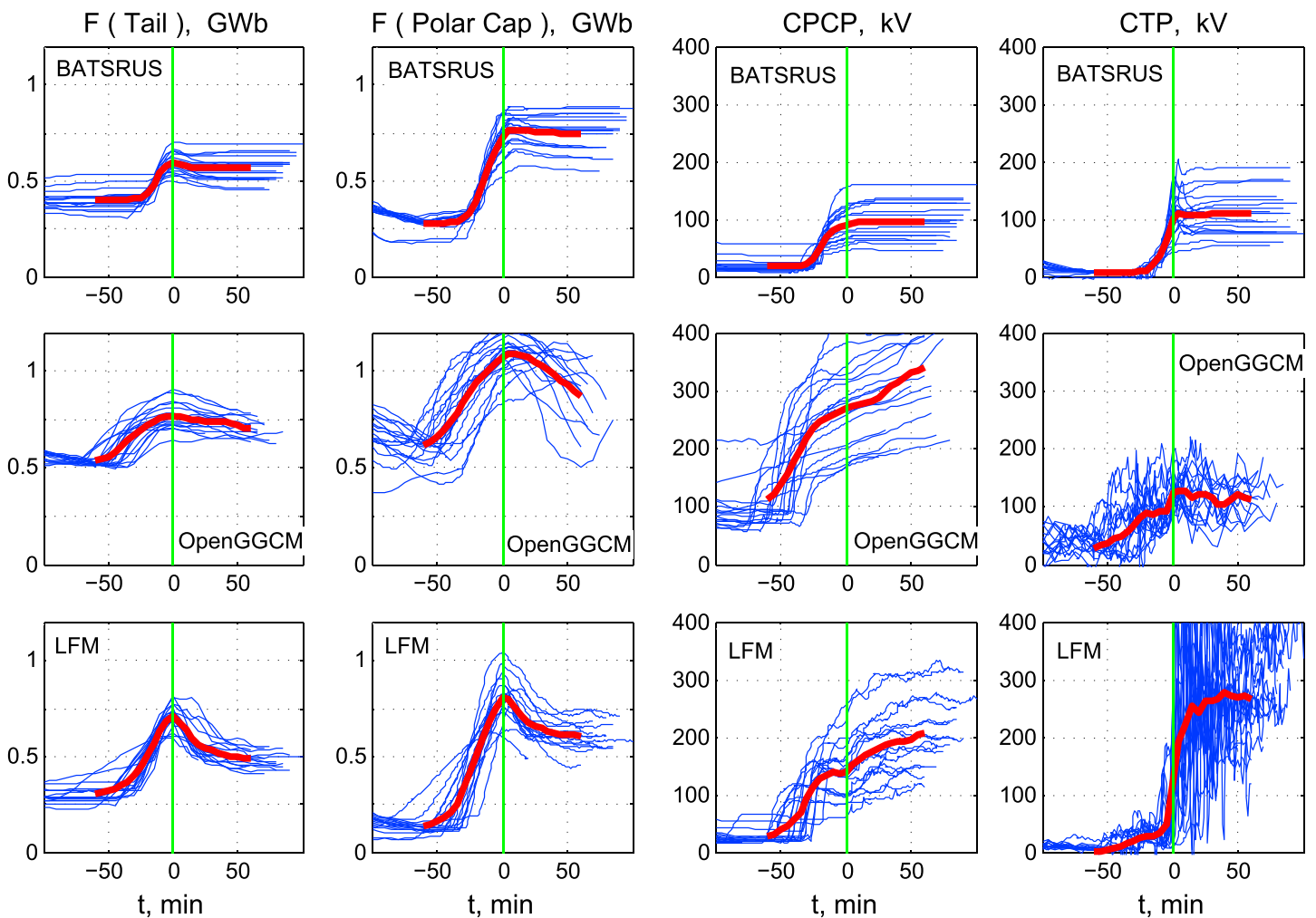
Figure 4. Superposed epoch analysis of (left column) tail magnetic flux and (right column) cross-tail potential behavior in three GMHD models. $T = 0$ epoch corresponds to the beginning of F_T unloading.

There are a few statistical studies of tail magnetic flux variations during substorms to be compared with the GMHD simulation results. Analyses of in situ evaluated magnetotail flux estimated using two-spacecraft based method [*Shukhtina et al.*, 2016] demonstrates a 41% magnetic flux decrease (from 0.82 to 0.48 GWb during ~60 min) for 110 substorm events [*Shukhtina et al.*, 2014]. One should caution that selection of substorms in this study was based on intense unloading signature, so this may provide rather an upper estimate of the average change. Other statistical studies are based on the polar cap magnetic flux (F_{PC}) evaluated from the imager data. The statistical results of magnetic flux variation known to us [*DeJong et al.*, 2007; *Huang et al.*, 2009; *Milan et al.*, 2009; *Shukhtina et al.*, 2014; *Walach and Milan*, 2015] are presented in Table 1. They show that although the average values of F_T (or F_{PC}) may vary, all authors consistently show large 20% to 40% magnetic flux unloading amplitude during the 55–85 min duration of the substorm expansion. Comparing these numbers with the unloading amplitude in the GMHD simulations (last three rows in Table 1), we must conclude that only LFM model provides a comparable unloading (31%) closely resembling the substorm expansion,

Table 1. Average Unloading of the Magnetotail Magnetic Flux During the Substorm Expansion

#	F, GWb (Onset)		F, GWb (Minimum)		Normalized Unloading Amplitude, %		Δt, Minutes (Unloading Duration)	Number of Substorms Used	Reference
	F_T	F_{PC}	F_T	F_{PC}	F_T	F_{PC}			
1		0.68		0.47		30%	54	31	*DeJong et al.* [2007]
2		0.68		0.50		27%	68	30	*Huang et al.* [2009]
3a		0.72		0.50		31%	~80	9	*Milan et al.* [2009 (iii-sbs)]
3b		0.86		0.50		42%	~85	10	*Milan et al.* [2009 (iv-sbs)]
4	0.82		0.48		41%		60	110	*Shukhtina et al.* [2014]
5		0.50		0.40		20%	60	4083	*Walach and Milan* [2015]
6	0.60	0.77	0.57	0.75	5%	3%	15	19	BATS-R-US (this study)
7	0.77	1.10	0.71	0.87	8%	21%	60	18	Open GGCM (this study)
8	0.71	0.80	0.49	0.61	31%	24%	50	19	LFM (this study)

Figure 5. Superposed epoch analysis (from left to right) of: tail magnetic flux, polar cap magnetic flux, cross-polar cap potential, and cross-tail potential. $T = 0$ epoch corresponds to the beginning of F_T unloading.

whereas the removal of the tail magnetic flux in BATS-R-US and Open GGCM simulations is rather small, being only 5% and 8%, respectively, and looks more like a smooth transition to the SMC mode.

The amount of magnetic flux unloading is closely related to the level of magnetotail convection (Φ_{PS} in Figure 1), which is represented by the CTP parameter. In LFM model the CTP displays a sharp increase near the $T = 0$ time from ~30 kV to ~280 kV, which indicates a strongly enhanced flux return rate (earthward convection) and provides rapid magnetotail unloading according to equation (3a). In BATS-R-US model the CTP value reaches only ~110 kV and in Open GGCM ~130 kV that is apparently not enough for significant unloading (in these cases CTP ≤ CPCP values, so $\Phi_{MP} \sim \Phi_{PS}$ and dF_T/dt are small).

An extended view of the global behavior is provided by Figure 5. In addition to magnetic flux and plasma sheet convection in the tail it also includes the parameters routinely evaluated at the ionospheric level at the CCMC, namely, the polar cap magnetic flux (F_{PC}) and the cross-polar cap potential (CPCP). Comparison of the magnetic fluxes generally shows qualitatively similar time variations of F_T and F_{PC}; however, the F_{PC} amplitude is systematically larger than the F_T amplitude at the end of growth phase: the average difference is about 40% for BATS-R-US and Open GGCM models, and it is about 10% for LFM. Such a large difference is a puzzle, its possible origins are discussed in the next section.

Significant differences between different models are also evident when comparing the ionospheric (CPCP) and cross-tail (CTP) potentials. In case of BATS-R-US model they are of nearly the same magnitude (roughly 100 kV), and the increase in CTP potential follows with ~25 min time delay after the CPCP increase, consistent with a short 25 min growth phase in the lobe magnetic flux. The BATS-R-US actually yields a smooth transition to a new balanced state, but with enhanced convection level (that is, a steady convection event). The Open GGCM results are very different and unexpected: the plasma sheet potential is 2–3 times smaller compared to the ionospheric potential (which by a factor of ~3 overestimates observational data, see Figure 8 in G15 paper). Finally, the LFM model displays, both qualitatively and quantitatively, a different relationship: during the growth phase the CPCP increases up to ~150 kV (still larger than in reality, see Figure 8 in G15 paper), while CTP remains at ~30 kV level. As discussed before, this situation ($\Phi_{MP} \gg \Phi_{PS}$ in Figure 1a) provides the most effective loading of magnetic flux into the tail. During the expansion phase, the relationship is opposite: here CTP jumps by an order of magnitude and this situation ($\Phi_{MP} \ll \Phi_{PS}$) provides effective unloading from the tail and enhanced convection and energy dissipation in the tail plasma sheet.

5. Discussion and Concluding Remarks

Global MHD models demonstrated their important role in Space Weather as an efficient physics-based research and prediction tool. Substorms are an important part of Space Weather: they are significant contributors to the ring current and radiation belt populations [*Gkioulidou et al.*, 2014; *Jaynes et al.*, 2015] and a factor of central importance in the energetic particle precipitation into the ionosphere. Their diverse space weather applications were recently demonstrated to also include significant effects on the upper atmosphere [*Clausen et al.*, 2014] and even on the middle atmosphere, including ozone depletion [*Seppala et al.*, 2015]. A very special role of substorms is due to high peak values of *E* field generated during the unloading phase in the tail reconnection and BBF generation processes, operated in localized parts of the magnetotail [*Semenov and Sergeev*, 1981; *Baker et al.*, 1996]. These high (inductive) *E* fields provide effective particle acceleration as well as their inward injection and precipitation [*Birn et al.*, 2012]. Therefore, it is crucially important for Space Weather applications to find out how well the global MHD codes reproduce the loading-unloading cycle and large plasma sheet *E* fields during the unloading phase.

One purpose of G15 and this paper was to demonstrate what a CCMC user would get after having launched an idealized simulation with 2 h of northward IMF followed by 2 h of southward IMF using the CCMC run-on-request system? And also, are there systematic differences between the answers provided by different GMHD models with the same inputs? It was shown in G15 that four CCMC-supported GMHD models are able, in general, to successfully reproduce the global magnetospheric equilibria in the wide range of input SW/IMF parameters. Here we emphasize, however, that a fundamental systematic difference exists in the dynamical response of these models to the same north-to-south IMF variation, aimed to simulate the loading-unloading sequence. We found that the LFM manifests a clear difference between the substorm phases, with depressed convection in the tail plasma sheet during the growth phase and sharp (an order of magnitude) enhancement of convection level during the expansion phase, which fits to the classical substorm concept and agrees with experimentally observed magnetic flux changes during isolated substorms (Figure 3). In contrast, in the
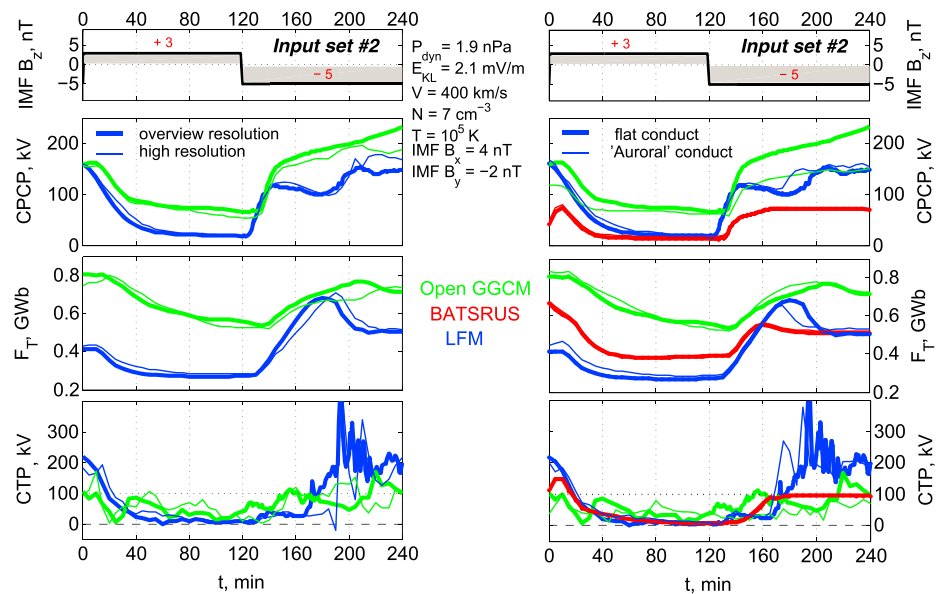
Figure 6. Comparison of integral parameters obtained in simulation #02 with (left) overview (medium) and high spatial grid resolution, (right) flat and "Auroral conductivity" model.

BATS-R-US and Open GGCM simulations a gradual enhancement of the magnetotail convection starts from the very beginning of global convection cycle induced by southward IMF, so it rather resembles a smooth transition from the quiet state to steady magnetospheric convection. Such a different system behavior also results in a big quantitative difference in the basic global dynamical characteristics, such as the rate and amount of loaded and unloaded magnetic flux, and the duration of the growth and expansion phases. The difficulty of reproducing the transient response in BATS-R-US simulations has been previously noticed by *Kuznetsova et al.* [2007], who found that inclusion of nongyrotropic corrections is necessary to get the dynamic quasiperiodic response to the steady driving conditions. In this respect we emphasize once more, that our validation results characterize the pure MHD component of global models (without merged kinetic modules) and that, in general, the incorporation of kinetic effects in some parts of the computation domain may certainly influence the system behavior.

One of the important technical aspects of numerical modeling is the spatial resolution, which controls the numerical effects (such as the numerical diffusion) and can significantly affect the solution. In our approach we tried to run models at comparable resolution, but this appeared to be difficult to realize because of different grid organization in the models (see, e.g., Table S1 in the supporting information). Also, the time costs of the massive computations in this project forced us to set the medium resolution for all simulations. So the question of how the results are changed with the increasing grid resolution needs to be addressed. For this purpose, we performed the simulation run #02 with twice higher resolution for the LFM ($106\times96\times128$ instead $53 \times 48 \times 64$ cells) and Open GGCM (9M instead 3.5M cells). Note, the BATS-R-US simulations were initially performed with the best spatial resolution routinely available at CCMC for that moment (2M cells). Comparing the high- and medium-resolution runs did not reveal any fundamental difference in the integral parameter values and behavior (Figure 6). The high-resolution simulations in both LFM and Open GGCM models showed little difference in details of the loading-unloading sequence and yielded a somewhat lower loading rates and slightly delayed times of the reconnection intensifications (which brings the LFM parameters somewhat closer to their experimental values, cf. Figure 3).

Another critical point is the choice of ionospheric conductance model that can potentially affect the magnetospheric dynamics [*Raeder et al.*, 2001]. To validate our results, obtained from simulations with a flat ionospheric conductance, we performed an additional simulation of the runs #02 with "auroral model" of ionospheric conductance [*Goodman*, 1995], which is dependent on UV solar irradiance as well as particle precipitation from the magnetosphere. The comparison shown in Figure 6 (left) demonstrates virtually identical values and behavior of CPCP, F_T and CTP parameters in BATS-R-US simulations with different ionospheric models. In the case of Open GGCM, the "auroral ionosphere" noticeably reduces the level of ionospheric and magnetotail

convection in self-similar manner leaving the magnetotail flux changes at the same level. In the LFM simulation with "auroral conductance" the only change is the 10 min earlier development of the substorm expansion as compared to the case with flat conductance.

Both spatial resolution and the ionospheric conductance model can modify the simulated magnetospheric response. However, the main global-scale dynamical features the large difference between the average convection level during the growth and expansion phases in the LFM simulation, the absence of such a big difference in the Open GGCM simulations and the smooth transition between two steady configurations in BATS-R-US remain the same.

The large difference between the values and variation amplitudes of the polar cap (F_{PC}) and tail (F_T) magnetic fluxes in Figure 5 is an unexpected result, which (to some extent) may influence the interpretation, so it also requires some explanation and discussion. Such a disagreement may have both natural (physics-related) reasons or be due to numerical artifacts. As concerns the natural reasons, the compared fluxes can indeed be different: the magnetic flux in the tail cross section at $X = -15 R_E$ certainly include the flux closed at larger tailward distances (which nominally does not contribute to F_{PC}), while, at the same time, the F_{PC} includes the newly reconnected (open) flux that permeates through the magnetopause between the cusp (say, at $X = 0$) and the tail cross section of interest (at $X = -15 R_E$), which is not counted in the F_T calculation and may increase F_{PC} in excess of F_T. This additional flux is readily evaluated as $F_{rec} = \Phi_D \cdot \Delta X / V_{SW}$, where Φ_D is the dayside reconnection rate. Taking $\Delta X = 15 R_E$, $V_{SW} = 400$ km/s, and $\Phi_D = 100$ kV, the newly opened flux penetrating through the magnetopause is $F_{rec} = 10^5 \cdot (15 \cdot 6400)/400 = 0.024$ GW. This estimate is by an order of magnitude smaller than the difference between F_{PC} and F_T variations in Figure 5 (being as large as 0.2 GWb and 0.3 GWb for BATS-R-US and Open GGCM), so this reasoning can hardly explain the magnetic flux discrepancy in these models.

Other sources of the discrepancy between F_{PC} and FT values can be related to some technical problems, such as precision of the boundary determination. First is a low precision of magnetotail boundary determination when calculating tail magnetic flux, which is hardly to be the case if using the mass flux method (see more about it and its comparison to other methods in Appendix A). The difference between the integrated tail magnetic flux, calculated using the magnetopause obtained from the mass flux method and from the fluopause method, rarely exceed 10% (which gives an upper estimate of F_T error due to inaccurate magnetopause determination).

The violation of div$B = 0$ and resulting magnetic flux loss in the plasma tube (see Appendix C) nominally should not contribute to the discussed discrepancy: OpenGGCM and LFM models exploit the constrained transport scheme to ensure that div$B = 0$ condition is fulfilled automatically, the BATS-R-US model operated at CCMC includes some divergence cleaning tools to remove the unphysical part of the magnetic field accumulated during the simulation (we note, however, that user should ensure that this option is switched on at the run-on-request system by contacting CCMC staff). However, the second potential source of discrepancy is the magnetic field interpolation errors, which can influence the accuracy of magnetic field line mapping and the polar cap boundary location, as well as some other postprocessing procedures. Some evidence of that is presented in Appendix C, demonstrating that computations using simple B field interpolation methods (which are also implemented at CCMC) results in unexpected effects like a magnetic flux loss/gain in the magnetotail magnetic flux tube or generation of nonzero div$B$, etc. Such numerical artifacts may also influence the accuracy of a number of magnetic field-based postprocessing procedures, like magnetic field line mapping or flux tube volume and entropy calculation, as well as the determination of the polar cap boundary (which is defined as the ionospheric mapping of open/closed field line topological boundary), etc. As this may significantly impact the interpretation of GMHD data, this issue definitely needs attention of both developers and the CCMC.

The origin of the other discrepancy in the above discussed large difference between the average ionospheric and plasma sheet electric potential drops in the Open GGCM simulation remains yet unclear. According to the Faraday's law (equation (3)), such a difference (average CPCP ~200–300 kV versus average CTP ~130 kV, during post onset intervals) should result in a considerable magnetic flux accumulation during both growth and expansion phases, which is actually not observed in the simulations. Alternatively, such a discrepancy would require large (50–100 kV) potential drops along magnetic field lines, in order to electrically decouple the ionosphere from the magnetosphere.

As a final remark, we realize that, first, there can be a number of hidden adjusting parameters that control the codes performance and, second, the described problems may refer to only their publicly available versions operated at the CCMC. However, we nevertheless find it important to diagnose and discuss these issues from the user's perspective.

To conclude, as a follow-up study to *Gordeev et al.* [2015], we tested in this paper the ability of three community-available GMHD magnetospheric models operated by NASA CCMC to reproduce the fundamental and observationally well-established substorm-related global cycle of the magnetic flux loading-unloading, initiated by the southward turning of the IMF. Our main findings are as follows:

1. Being tested with a comparable grid resolution and using the same set of 19 input sequences with north-to-south IMF turning, three CCMC-supported models displayed a systematically different global behavior. Among those models, the LFM displayed the generic substorm-like behavior of mutually related tail magnetic flux variations (dF_T/dt), the dayside merging-induced tailward convection (CPCP), and the return convection (CTP), as known from observations and summarized in phenomenological near-Earth neutral line model [*McPherron*, 1991; *Baker et al.*, 1996], are most clearly manifested by the LFM model. Only for that model the return convection is depressed and the loading rate is high during the growth phase, whereas the return convection is enhanced and unloading rate is high during the expansion phase. Quantitatively, the amount of loaded/unloaded magnetotail flux and the growth phase duration in the LFM were closest to their values empirically observed for the isolated substorms. Two other models showed a drastically different behavior, with the BATS-R-US plasma sheet convection exhibiting a smooth transition to the steady convection regime after the IMF southward turning, while the Open GGCM showed rather weak plasma sheet convection (CTP smaller than CPCP) with comparable intensities during the growth and expansion phases.

2. Our investigation also identified potential problems in postprocessing calculations based on the routinely interpolated values of simulated magnetic fields. This includes a noticeable nonzero div*B* based on interpolated magnetic field and a loss of magnetic flux in the magnetic flux tube, signaling on the errors which may affect the accuracy of magnetic field tracing and calculation of such parameters as polar cap area, magnetic tube volume, and others. Final evaluation of the severity of discovered problems as well as solving them is beyond the scope of our study as it will require concerted efforts on the part of the developers, CCMC staff, and the users community.

Appendix A: Fast Computation of the Simulated Tail Magnetopause and Magnetic Flux

To calculate the magnetic flux through the *YZ* cross section of the magnetotail, one needs to integrate the *X* component of the magnetic field over that section, that is, evaluate $F_T = \int_S B_x ds$. To determine the magnetopause position, we use a fast and robust method by *Peng et al.* [2010], based on the particle mass flux. Its essence is to find a surface where the mass flux mNV becomes twice smaller than the solar wind mass flux $mN_{SW}V_{SW}$. This simple procedure gives an adequate proxy for the tailward magnetopause position.
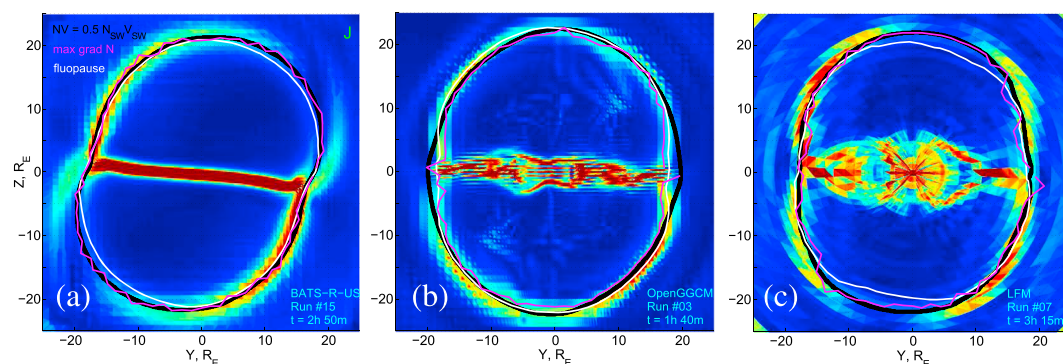
Figure A1. Examples of comparing four methods to define the magnetopause in (a) BATS-R-US, (b) Open GGCM, and (c) LFM simulation, including the current density peak (shown by color distribution), density gradient maximum (magenta), fluopause (white), and mass flux (black) methods.
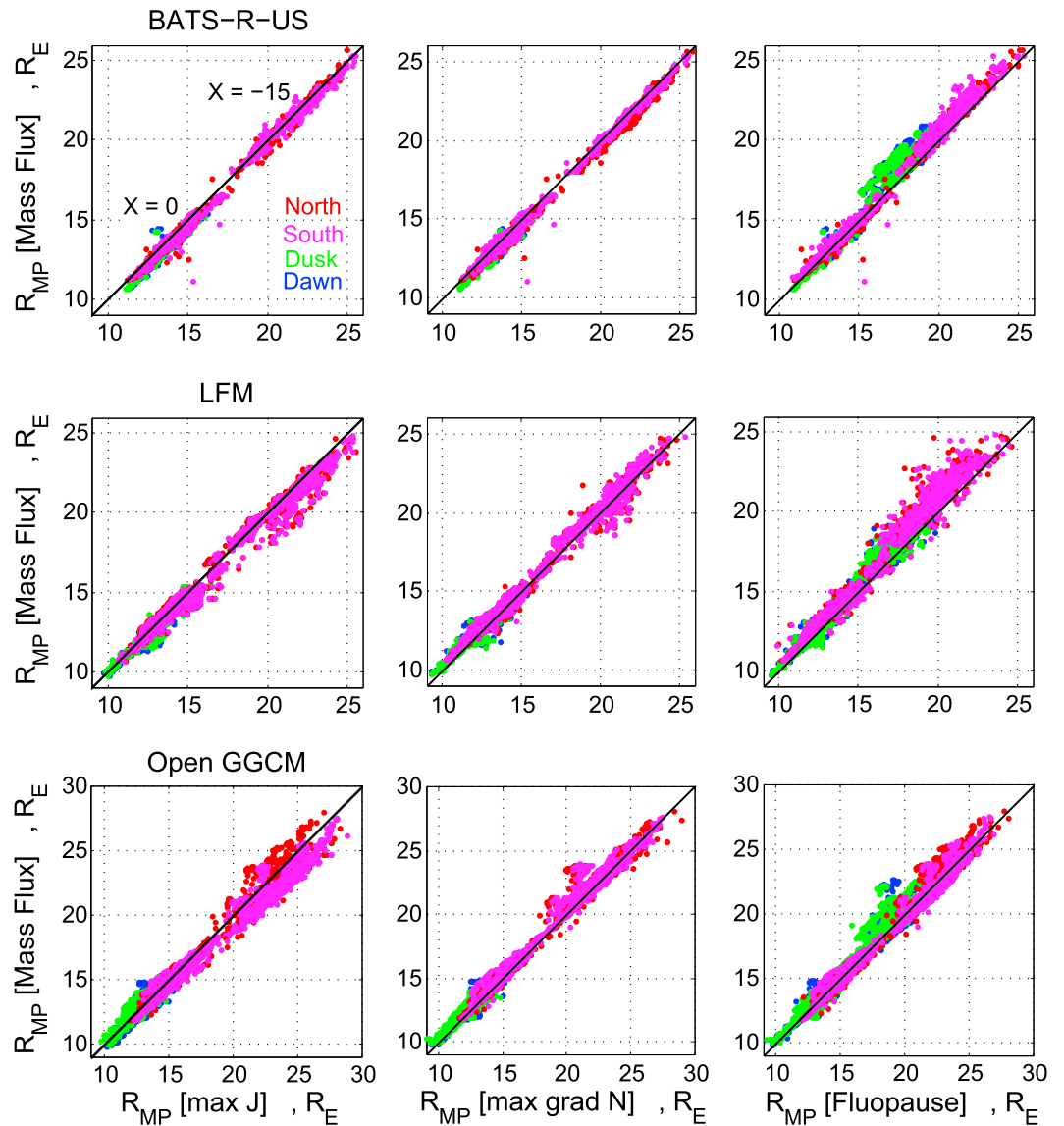
Figure A2. Comparison of the magnetopause locations obtained by the mass flux method with those based on the (left column) electric current peak and (middle column) density gradient local methods, as well as with the (right column) nonlocal fluopause method. The scatterplots combine the data at terminator ($X = 0$) and midtail ($X = -15 R_E$) cross sections, color coded for the four magnetopause segments: north (red), south (magenta), dusk (green), and dawn (blue). Each R_{MP} position is calculated as the magnetopause distance averaged over 15° angle.

For illustration, we show the magnetopause proxies at $X = -15 R_E$ determined by four different methods (Figure A1). These examples demonstrate a good agreement between the magnetopause proxy based on the mass flux and those obtained by local methods using both the current density peak and the maximum of the density gradient. Note that the fluopause is located up to several R_E further inside the tail.

To check the accuracy of the suggested magnetopause proxy, we performed a systematic comparison with three other methods using all our set of 19 runs for each of three GMHD models. The scatterplots in the Figure A2 confirm a nice correspondence between all magnetopause proxies in the terminator ($X = 0$) cross section both for high- and low-latitude magnetopause. In the midtail ($X = -15 R_E$) the mass flux method is in good agreement with both local maxJ and maxgradN methods, while the fluopause appears $1-2 R_E$ closer to the Sun-Earth line, except for the Open GGCM, which shows comparable results between all proxies including the fluopause. Note that in the low-latitude midtail region the gradients of MHD variables are usually too

small, so that maxJ and maxgradN methods become unreliable. For that reason, at $X = -15\,R_E$ we use only the high-latitude portions of the magnetopause in the comparison.

Based on the above results, we chose in this study the mass flux reduction method to identify the magnetopause, which is local, computationally cheap, yields a smooth and well-defined surface at both high and low latitudes, and agrees quite well with the other local methods.

Once the magnetopause position is determined, it is easy to calculate the tail magnetic flux by integrating B_x over the area bounded by the magnetopause. Separation of the magnetic fluxes belonging to the northern/southern lobes was done according to the positive/negative sign of B_x (in the GSM system). The magnetopause contour was then approximated by a spline, and contributions from the boundary cells were taken into account.

Appendix B: Empirical Data Characterizing the Substorm Growth Phase Parameters

The procedure to find the GP parameters was, briefly, as follows (more details will be published elsewhere). First, we performed a global search of 5 min averaged OMNI data for years 2001–2014 to identify the events which had >1.5 h northward IMF ($B_z > 0.5$ nT, up to two records with data gaps or spikes were allowed) followed by >1.5 h southward IMF ($B_z < -0.5$ nT). From them we deleted events that had a continued activity ($AL < -100$ nT) throughout the interval, as well as those which had no distinct PC index enhancement associated with the southward IMF turning. The data selection resulted in 218 events with clear PC index onsets, which were assumed as the actual onsets of convection enhancement in the magnetosphere, that is—the growth phase onsets. For them we scanned the SuperMAG substorm onset database [*Newell and Gjerloev*, 2011] and found 122 SuperMAG onsets on the nightside available for our study of growth phase duration as a function of the solar wind merging electric field E_{KL}. In 90 cases there were no SuperMAG onsets available (more than half of them were weak events), and six cases were discarded as wrong because of dayside location of the determining station. The range and distribution of the observed T_{GP} values as well as their decreasing trend with the increasing E_{KL} magnitude are similar to those found in previous studies [*Dmitrieva and Sergeev*, 1983; *Petrukovich*, 2000; *Li et al.*, 2013] and were used for testing the simulation results in section 3 (Figure 3a).

Determination of the tail lobe magnetic field increase and of the loading rate is more involved, and no reliable statistical results were published previously on the solar wind dependence of these parameters, except for the *Rybalchenko and Sergeev* [1985] study, based on a small statistics. For that purpose, we used 1 min resolution Cluster data at distances between -9 and $-20\,R_E$ and Geotail data at $r < 25\,R_E$, in which only low-beta samples ($2\mu_0 P/B^2 < 0.5$) were selected for the analysis, and the equivalent lobe magnetic field was defined as ($B_L = (B^2/2\mu_0 + P)^{1/2}$). Alternatively, a similar estimate, B_{ext}, based on the external B-field part (that is, with the IGRF contribution subtracted) was also computed, to avoid some interpretational difficulties in the inner magnetosphere (at $r < 12\,R_E$). Both B_L and B_{ext} were statistically analyzed in the same way (and the results were found to be similar). The next (difficult) task was to obtain the desired statistical dependence of ΔB_L (and $\Delta B_L/\Delta T$) on the solar wind merging E field by cleaning the B_L dependence on radial distance and on the solar wind flow pressure, using in both cases the statistical dependences derived by *Fairfield and Jones* [1996] (FJ96). First of all, we corrected the radial dependence effect by scaling B_L to $r = 15\,R_E$, based on spacecraft distance and using equation (3) of FJ96. To correct for the changes in solar wind dynamical pressure P_d, we computed the 5 min average lobe fields at $r = 15\,R_E$ for the OMNI-based P_d values (delayed by 5 min to account for the solar wind propagation to $X = -15\,R_E$) based on FJ96 formula. The difference of these values (taken at the end and start of time interval ΔT used to compute the loading rate) were then subtracted from the corresponding lobe field difference ΔB_L to get the corrected lobe change amplitude ΔB_L^{cr} and the loading rate $\Delta B_L^{cr}/\Delta T$. This is what we used for comparison with the simulation results in section 3 and Figure 3b.

Appendix C: Magnetic Field Divergence and Magnetic Flux Mapping in GMHD Models

The postprocessing analysis often includes interpolation of simulated parameter values, available only at discrete grid points. Some procedures require massive interpolation of initial values, an example being the magnetic field line tracing procedure. Here we discuss how big the interpolation errors can be in terms of the $\text{div}B = 0$ violation and by testing the magnetic flux conservation along the magnetic field line tubes.
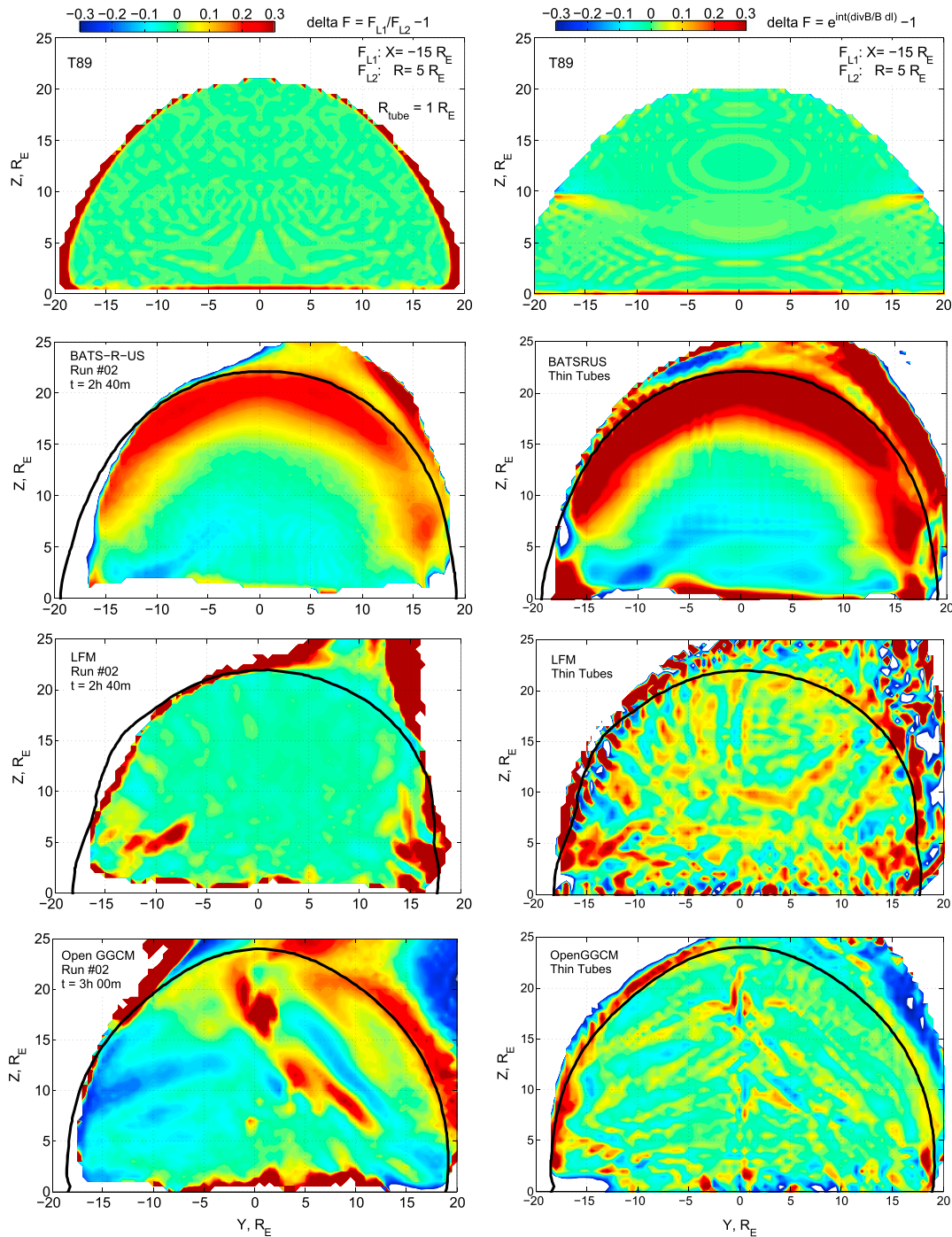
Figure C1. Color maps of the magnetic flux loss/gain along the tubes from $X = -15\,R_E$ cross section to $R = 5\,R_E$ spherical surface calculated by (left column) tracing the tubes with $r = 1\,R_E$ radius and (right column) integrating of div$B$ by equation (C5) in CCMC models obtained from results of the #02 runs. Magnetopause contour is shown by thick black line. The maps are constructed for the period of substorm expansion. Note that the integration does not eliminate the local effects of magnetic flux loss/gain. Note the extended areas of significant magnetic flux loss/gain in BATS-R-US simulations, possibly attributed to disabled div$B$ elimination during the simulation.

To obtain the field vector at an arbitrary location inside the 3-D grid, one has to separately interpolate the values of B_x, B_y, and B_z between the nearest nodes, which necessarily creates an artificial divergence, even if the original field had div$B = 0$. Indeed, the examination of interpolated magnetic fields in randomized points inside the magnetotail showed that the divergence, normalized by its highest possible value at the same location, $||\text{div}B|| = \text{div}B/(|\frac{\partial B_x}{\partial x}| + |\frac{\partial B_y}{\partial y}| + |\frac{\partial B_z}{\partial z}|)$, may often approach ± 1. It means that at such points

the variation of interpolated magnetic field is heavily contaminated by artificial interpolation errors. To assess the importance of the artificial div$B \neq 0$ in postprocessing, and to test if the integration along the field lines could eliminate the random errors, we developed two procedures to calculate the loss/gain of the magnetic flux (which should be precisely conserved in an ideal case) along a thin magnetic tube. The first procedure evaluates the direct contribution of nonzero div$B$ to the magnetic flux loss, while the second one evaluates the degree of the magnetic flux nonconservation by tracing field lines passing through a finite-size closed contour defining a flux tube.

Consider a short element dl of a thin magnetic field line tube with a cross section area d$S(l)$, the local field magnitude $B(l)$, and the corresponding flux

$$F(l) = B(l)\mathrm{d}S(l) \tag{C1}$$

Note from the outset that the interpolated magnetic field is not assumed hereto be perfectly divergenceless, i.e., div$B \neq 0$ and, hence, $F(l) \neq$ const. The flux gain along the tube element dl equals d$F = \mathrm{div}B(l) \cdot \mathrm{d}l \cdot \mathrm{d}S(l)$, which, on account of (C1), yields

$$\frac{\mathrm{d}F}{\mathrm{d}l} = \frac{F(l)}{B(l)}\mathrm{div}B(l) \tag{C2}$$

or

$$\frac{\mathrm{d}}{\mathrm{d}l}\ln F = \frac{\mathrm{div}B(l)}{B(l)} \tag{C3}$$

Integrating (C3) between starting point L_1 and arbitrary location L_2 gives

$$\ln\frac{F_{L1}}{F_{L2}} = \int_{L_1}^{L_2} \frac{\mathrm{div}B(l)}{B(l)}\mathrm{d}l \tag{C4}$$

or, in terms of the relative flux gain (loss) between L_1 and L_2:

$$\Delta F = \frac{F_{L1}}{F_{L2}} - 1 = \exp\left(\int_{L_1}^{L_2} \frac{\mathrm{div}B(l)}{B(l)}\mathrm{d}l\right) - 1 \tag{C5}$$

The examples of div$B$ integration using interpolated fields of three GMHD models and corresponding changes of magnetic flux along field lines between the tail cross section at $X = -15\,R_E$ and the spherical surface with radius $r = 5\,R_E$, are shown in Figure C1 (right column).

Also, to evaluate the magnetic flux losses along individual field line tubes, we traced the field lines from a set of 360 equidistant starting points lying on a circular contour of radius $1\,R_E$ at the $X = -15\,R_E$ cross section until they reach a sphere of radius $r = 5\,R_E$, concentric with the Earth's surface. The magnetic flux loss factor was calculated as the ratio of magnetic flux through the starting contour F_{L1} to that permeating the ending contour F_{L2}, $\Delta F = F_{L1}/F_{L2} - 1$ (Figure C1, left column).

Both procedures show large magnetic flux losses (often exceeding 20–30%) which can be generated in the extended areas of the tail cross section (Figure C1), even quite far from the magnetopause and thin current sheets. Similar results are systematically observed throughout the simulations.

Note that we tried two versions of the interpolation procedure (trilinear and tricubic interpolation), and both of them yielded virtually identical results. To estimate the accuracy of the interpolation procedures themselves, we substituted the simulated magnetic field with a perfectly divergenceless T89 model field [*Tsyganenko*, 1989], evaluated in the nodes of the same uniform 3-D interpolation grid with $0.5\,R_E$ spacing, res- olution, and applied the same tracing procedure based on the interpolated T89 field. The calculation results are shown in the same format in the top row of Figure C1. A closer inspection reveals that in the T89 case the absolute value of the normalized numerical div$B$ does not exceed 10^{-3}, and the magnetic flux is almost perfectly conserved along the flux tubes, except in a vicinity of the neutral sheet. A natural conclusion is that simple interpolation procedures do not pose any problem in case of smooth magnetic field distributions (like those in T89) but may result in uncontrolled large errors in the presence of sharp field gradients.

As a consequence, the nonzero divergence of interpolated magnetic fields can significantly distort the postprocessing calculations in the first-principle-based models [*Mackay et al.*, 2006] and especially of those characteristics that involve the field line tracing, such as the computations of the polar cap area, magnetic tube volume and entropy, magnetic field line mapping in the magnetosphere and in the ionosphere.

Final evaluation of the importance of discovered problems as well as their solution requires a concerted effort on the part of developers, CCMC staff, and the user's community.

References

Angelopoulos, V., A. Runov, X.-Z. Zhou, D. L. Turner, S. A. Kiehas, S.-S. Li, and I. Shinohara (2013), Electromagnetic energy conversion at reconnection fronts, *Science*, *341*, 1478–1482, doi:10.1126/science.1236992.

Ashour-Abdalla, M., G. Lapenta, R. J. Walker, M. El-Alaoui, and H. Liang (2015), Multiscale study of electron energization during unsteady reconnection events, *J. Geophys. Res. Space Physics*, *120*, 4784–4799, doi:10.1002/2014JA020316.

Baker, D. N., T. I. Pulkkinen, V. Angelopoulos, W. Baumjohann, and R. L. McPherron (1996), The neutral line model of substorms: Past results and present view, *J. Geophys. Res.*, *101*, 12,975–13,010.

Birn, J., A. Artemyev, D. Baker, M. Echim, M. Hoshino, and L. Zelenyi (2012), Particle acceleration in the magnetotail and aurora, *Space Sci. Rev.*, *173*, 49–102, doi:10.1007/s11214-012-9874-4.

Clausen, L. B. N., S. E. Milan, J. B. H. Baker, J. M. Ruohoniemi, K.-H. Glassmeier, J. C. Coxon, and B. J. Anderson (2013), On the influence of open magnetic flux on substorm intensity: Ground- and space-based observations, *J. Geophys. Res. Space Physics*, *118*, 2958–2969, doi:10.1002/jgra.50308.

Clausen, L. B. N., S. E. Milan, and A. Grocott (2014), Thermospheric density perturbations in response to substorms, *J. Geophys. Res. Space Physics*, *119*, 4441–4455, doi:10.1002/2014JA019837.

Cowley, S. W. H., and M. Lockwood (1992), Excitation and decay of solar wind driven flows in the magnetosphere–ionosphere system, *Ann. Geophys.*, *10*, 103–115.

Daldorff, L. K., G. Tóth, T. I. Gombosi, G. Lapenta, J. Amaya, S. Markidis, and J. U. Brackbill (2014), Two-way coupling of a global Hall magnetohydrodynamics model with a local implicit particle-in-cell model, *J. Comput. Phys.*, *268*, 236–254.

DeJong, A. D., X. Cai, C. R. Clauer, and J. F. Spann (2007), Aurora and open magnetic flux during isolated substorms, sawteeth, and SMC events, *Ann. Geophys.*, *25*, 1865–1876.

DeJong, A. D., A. J. Ridley, X. Cai, and C. R. Clauer (2009), A statistical study of BRIs (SMCs), isolated substorms, and individual sawtooth injections, *J. Geophys. Res.*, *114*, A08215, doi:10.1029/2008JA013870.

Dmitrieva, N. P., and V. A. Sergeev (1983), Spontaneous and induced beginning of the burst phase of a magnetospheric substorm and its preliminary phase duration [in Russian], *Geomagn. Aeron.*, *23*(3), 470–474.

Dmitrieva, N. P., V. A. Sergeev, and M. A. Shukhtina (2004), Average characteristics of the midtail plasma sheet in different dynamic regimes of the magnetosphere, *Ann. Geophys.*, *22*, 2107–2113.

Dungey, J. W. (1961), Interplanetary magnetic fields and the auroral zones, *Phys. Rev. Lett.*, *6*, 47–48.

Fairfield, D. H., and J. Jones (1996), Variability of the tail lobe field strength, *J. Geophys. Res.*, *101*(A4), 7785–7791, doi:10.1029/95JA03713.

Garcia, K. S., and W. J. Hughes (2007), Finding the Lyon-Fedder-Mobarry magnetopause: A statistical perspective, *J. Geophys. Res.*, *112*, A06229, doi:10.1029/2006JA012039.

Gkioulidou, M., A. Y. Ukhorskiy, D. G. Mitchell, T. Sotirelis, B. H. Mauk, and L. J. Lanzerotti (2014), The role of small-scale ion injections in the buildup of Earth's ring current pressure: Van Allen Probes observations of the 17 March 2013 storm, *J. Geophys. Res. Space Physics*, *119*, 7327–7342, doi:10.1002/2014JA020096.

Goodman, M. L. (1995), A three-dimensional, iterative mapping procedure for the implementation of an ionosphere-magnetosphere anisotropic Ohm's law boundary condition in global magnetohydrodynamic simulations, *Ann. Geophys.*, *13*, 843–853, doi:10.1007/s00585-995-0843-z.

Gordeev, E., V. Sergeev, I. Honkonen, M. Kuznetsova, L. Rastatter, M. Palmroth, P. Janhunen, G. Tóth, J. Lyon, and M. Wiltberger (2015), Assessing the performance of community-available global MHD models using key system parameters and empirical relationships, *Space Weather*, *13*, 868–884, doi:10.1002/2015SW001307.

Gordeev, E. I., V. A. Sergeev, T. I. Pulkkinen, and M. Palmroth (2011), Contribution of magnetotail reconnection to the cross-polarcap electric potential drop, *J. Geophys. Res.*, *116*, A08219, doi:10.1029/2011JA016609.

Honkonen, I., L. Rastatter, A. Grocott, A. Pulkkinen, M. Palmroth, J. Raeder, A. J. Ridley, and M. Wiltberger (2013), On the performance of global magnetohydrodynamic models in the Earth's magnetosphere, *Space Weather*, *11*, 313–326, doi:10.1002/swe.20055.

Huang, C.-S., A. D. DeJong, and X. Cai (2009), Magnetic flux in the magnetotail and polar cap during sawteeth, isolated substorms, and steady magnetospheric convection events, *J. Geophys. Res.*, *114*, A07202, doi:10.1029/2009JA014232.

Janhunen, P., M. Palmroth, T. V. Laitinen, I. Honkonen, L. Juusola, G. Facsko, and T. I. Pulkkinen (2012), The GUMICS-4 global MHD magnetosphere-ionosphere coupling simulation, *J. Atmos. Sol. Terr. Phys.*, *80*, 48–59, doi:10.1016/j.jastp.2012.03.006.

Jaynes, A. N., et al. (2015), Source and seed populations for relativistic electrons: Their roles in radiation belt changes, *J. Geophys. Res. Space Physics*, *120*, 7240–7254, doi:10.1002/2015JA021234.

Kuznetsova, M. M., M. Hesse, L. Rastätter, A. Taktakishvili, G. Tóth, D. L. De Zeeuw, A. Ridley, and T. I. Gombosi (2007), Multiscale modeling of magnetospheric reconnection, *J. Geophys. Res.*, *112*, A10210, doi:10.1029/2007JA012316.

Li, H., C. Wang, and Z. Peng (2013), Solar wind impacts on growth phase duration and substorm intensity: A statistical approach, *J. Geophys. Res. Space Physics*, *118*, 4270–4278, doi:10.1002/jgra.50399.

Lyon, J. G., J. A. Fedder, and C. M. Mobarry (2004), The Lyon-Fedder-Mobarry (LFM) global MHD magnetospheric simulation code, *J. Atmos. Sol. Terr. Phys.*, *66*(15–16), 1333–1350, doi:10.1016/j.jastp.2004.03.020.

Mackay, F., R. Marchand, and K. Kabin (2006), Divergence-free magnetic field interpolation and charged particle trajectory integration, *J. Geophys. Res.*, *111*, A06205, doi:10.1029/2005JA011382.

McPherron, R. L. (1991), Physical processes producing magnetospheric substorms and magnetic storms, in *Geomagnetism*, vol. 4, edited by J. Jacobs, pp. 593–739, Academic Press, London.

Merkin, V. G., and J. G. Lyon (2010), Effects of the low-latitude ionospheric boundary condition on the global magnetosphere, *J. Geophys. Res.*, *115*, A10202, doi:10.1029/2010JA015461.

Milan, S. E., G. Provan, and B. Hubert (2007), Magnetic flux transport in the Dungey cycle: A survey of dayside and nightside reconnection rates, *J. Geophys. Res.*, *112*, A01209, doi:10.1029/2006JA011642.

Milan, S. E., A. Grocott, C. Forsyth, S. M. Imber, P. D. Boakes, and B. Hubert (2009), A superposed epoch analysis of auroral evolution during substorm growth, onset and recovery: Open magnetic flux control of substorm intensity, *Ann. Geophys.*, *27*, 659–668, doi:10.5194/angeo-27-659-2009.

Nakamura, R., L. F. Bargatze, T. Mukai, T. Nagai, K. B. Baker, M. R. Hairston, P. H. Reiff, A. A. Petrukovich, M. Nozdrachev, and O. A. Troshichev (1999), Response of the midtail electric field to enhanced solar wind energy input, *J. Geophys. Res.*, *104*, 17,299–17,310, doi:10.1029/1999JA900166.

Newell, P. T., and J. W. Gjerloev (2011), Substorm and magnetosphere characteristic scales inferred from the SuperMAG auroral electrojet indices, *J. Geophys. Res.*, *116*, A12232, doi:10.1029/2011JA016936.

Palmroth, M., T. I. Pulkkinen, P. Janhunen, and C.-C. Wu (2003), Stormtime energy transfer in global MHD simulation, *J. Geophys. Res.*, *108*(A1), 1048, doi:10.1029/2002JA009446.

Pembroke, A., F. Toffoletto, S. Sazykin, M. Wiltberger, J. Lyon, V. Merkin, and P. Schmitt (2012), Initial results from a dynamic coupled magnetosphere-ionosphere-ring current model, *J. Geophys. Res.*, *117*, A02211, doi:10.1029/2011JA016979.

Peng, Z., C. Wang, and Y. Q. Hu (2010), Role of IMF B_x in the solar wind-magnetosphere-ionosphere coupling, *J. Geophys. Res.*, *115*, A08224, doi:10.1029/2010JA015454.

Petrukovich, A. A. (2000), The growth phase: Comparison of small and large substorms, in *Proc. 5th International Conference on Substorms (ICS-5)*, edited by A. Wilson, pp. 9–14, European Space Agency, St. Petersburg, Russia.

Pilipp, W. G., and G. Morfill (1978), The formation of the plasma sheet resulting from plasma mantle dynamics, *J. Geophys. Res.*, *83*, 5670–5678, doi:10.1029/JA083iA12p05670.

Powell, K. G., P. L. Roe, T. J. Linde, T. I. Gombosi, and D. L. De Zeeuw (1999), A solution-adaptive upwind scheme for ideal magnetohydrodynamics, *J. Comput. Phys.*, *154*, 284–309, doi:10.1006/jcph.1999.6299.

Provan, G., M. Lester, S. B. Mende, and S. E. Milan (2004), Statistical study of high-latitude plasma flow during magnetospheric substorms, *Ann. Geophys.*, *22*, 3607–3624, doi:10.5194/angeo-22-3607-2004.

Pulkkinen, A., et al. (2011), Geospace environment modeling 2008–2009 challenge: Ground magnetic field perturbations, *Space Weather*, *9*, S02004, doi:10.1029/2010SW000600.

Raeder, J., R. L. McPherron, L. A. Frank, S. Kokubun, G. Lu, T. Mukai, W. R. Paterson, J. B. Sigwarth, H. J. Singer, and J. A. Slavin (2001), Global simulation of the Geospace Environment Modeling substorm challenge event, *J. Geophys. Res.*, *106*(A1), 381–395, doi:10.1029/2000JA000605.

Raeder, J., D. Larson, W. Li, E. L. Kepko, and T. Fuller-Rowell (2008), OpenGGCM simulations for the THEMIS mission, *Space Sci. Rev.*, *141*(1–4), 535–555, doi:10.1007/s11214-008-9421-5.

Russell, C. T., and R. L. McPherron (1973), The magnetotail and substorms, *Space Sci. Rev.*, *15*, 205–266, doi:10.1007/BF00169321.

Rybalchenko, V. V., and V. A. Sergeyev (1985), Rate of magnetic flux buildup in the magnetospheric tail, *Geomagn. Aeron.*, *25*, 378–385, (Engl. Transl).

Semenov, V. S., and V. A. Sergeev (1981), A simple semi-empirical model for the magnetospheric substorm, *Planet. Space Sci.*, *29*, 271–281.

Seppala, A., M. A. Clilverd, M. J. Beharrell, C. J. Rodger, P. T. Verronen, M. E. Andersson, and D. A. Newnham (2015), Substorm-induced energetic electron precipitation: Impact on atmospheric chemistry, *Geophys. Res. Lett.*, *42*, 8172–8176, doi:10.1002/2015GL065523.

Shukhtina, M. A., N. P. Dmitrieva, N. G. Popova, V. A. Sergeev, A. G. Yahnin, and I. V. Despirak (2005), Observational evidence of the loading-unloading substorm scheme, *Geophys. Res. Lett.*, *32*, L17107, doi:10.1029/2005GL023779.

Shukhtina, M. A., N. P. Dmitrieva, and V. A. Sergeev (2014), On the conditions preceding sudden magnetotail magnetic flux unloading, *Geophys. Res. Lett.*, *41*, 1093–1099, doi:10.1002/2014GL059290.

Shukhtina, M. A., E. I. Gordeev, V. A. Sergeev, N. A. Tsyganenko, L. B. N. Clausen, and S. E. Milan (2016), Magnetotail magnetic flux monitoring based on simultaneous solar wind and magnetotail observations, *J. Geophys. Res. Space Physics*, *121*, 8821–883, doi:10.1002/2016JA022911.

Siscoe, G. L., and T. S. Huang (1985), Polar cap inflation and deflation, *J. Geophys. Res.*, *90*, 543–547.

Siscoe, G. L., G. M. Erickson, B. U. Sonnerup, N. C. Maynard, K. D. Siebert, D. R. Weimer, and W. W. White (2001), Global role of E in magnetopause reconnection: An explicit demonstration, *J. Geophys. Res.*, *106*, 13,015–13,022, doi:10.1029/2000JA000062.

Toffoletto, F., S. Sazykin, R. Spiro, and R. Wolf (2005), Inner magnetospheric modeling with the Rice Convection Model, *Space Sci. Rev.*, *107*(1–2), 175–196, doi:10.1023/A:1025532008047.

Toth, G., et al. (2012), Adaptive numerical algorithms in space weather modeling, *J. Comput. Phys.*, *231*(3), 870–903.

Tsyganenko, N. A. (1989), A magnetospheric magnetic field model with a warped tail current sheet, *Planet. Space Sci.*, *37*(1), 5–20.

Walach, M.-T., and S. E. Milan (2015), Are steady magnetospheric convection events prolonged substorms?, *J. Geophys. Res. Space Physics*, *120*, 1751–1758, doi:10.1002/2014JA020631.

Wang, C., J. P. Han, H. Li, Z. Peng, and J. D. Richardson (2014), Solar wind-magnetosphere energy coupling function fitting: Results from a global MHD simulation, *J. Geophys. Res. Space Physics*, *119*, 6199–6212, doi:10.1002/2014JA019834.

Wang, C.-P., L. R. Lyons, and V. Angelopoulos (2014), Properties of low-latitude mantle plasma in the Earth's magnetotail: ARTEMIS observations and global MHD predictions, *J. Geophys. Res. Space Physics*, *119*, 7264–7280, doi:10.1002/2014JA020060.

Yahnin, A. G., I. V. Despirak, A. A. Lubchich, B. V. Kozelov, N. P. Dmitrieva, M. A. Shukhtina, and H. K. Biernat (2006), Relationship between substorm auroras and processes in the near-Earth magnetotail, *Space Sci. Rev.*, *122*, 97–106, doi:10.1007/s11214-006-5884-4.

Zhang, Q.-H., M. Lockwood, J. C. Foster, S.-R. Zhang, B.-C. Zhang, I. W. McCrea, J. Moen, M. Lester, and J. M. Ruohoniemi (2015), Direct observations of the full Dungey convection cycle in the polar ionosphere for southward interplanetary magnetic field conditions, *J. Geophys. Res. Space Physics*, *120*, 4519–4530, doi:10.1002/2015JA021172.